Supporting Information for

[North Atlantic and the Barents Sea Variability Contribute to the 2023 Extreme Fire Season in Canada]

[Guanyu Liu[1], Jing Li[1*], Xichen Li[2], Tong Ying[1]]

[[1] Department of Atmospheric and Oceanic Sciences, School of Physics, Peking University, Beijing, China]

[[2] Institute of Atmospheric Physics, Chinese Academy of Sciences, Beijing, China]

Contents of this file

Table S1 List of the CMIP6 models, experiments, and the number of ensemble members of AMIP experiments analyzed in this study

Model	Number	Reference
ACCESS-ESM1-5	3	Ziehn et al., 2019
BCC-CSM2-MR	3	Wu et al., 2018
CESM2	10	Danabasoglu, 2019
CNRM-CM6-1	1	Vordoire, 2018
CanESM5	7	Swart et al., 2019
FGOALS-g3	5	Li, 2019
GFDL-ESM4	1	Krasting et al., 2018
GISS-E2-1-G	20	NASA/GISS, 2018
HadGEM3-GC31-LL	5	Ridley et al., 2019
IPSL-CM6A-LR	21	Boucher et al., 2018
MIROC6	10	Tatebe & Watanabe, 2018
MRI-ESM2-0	3	Yukimoto et al., 2019
NorESM2-LM	1	Seland et al., 2019

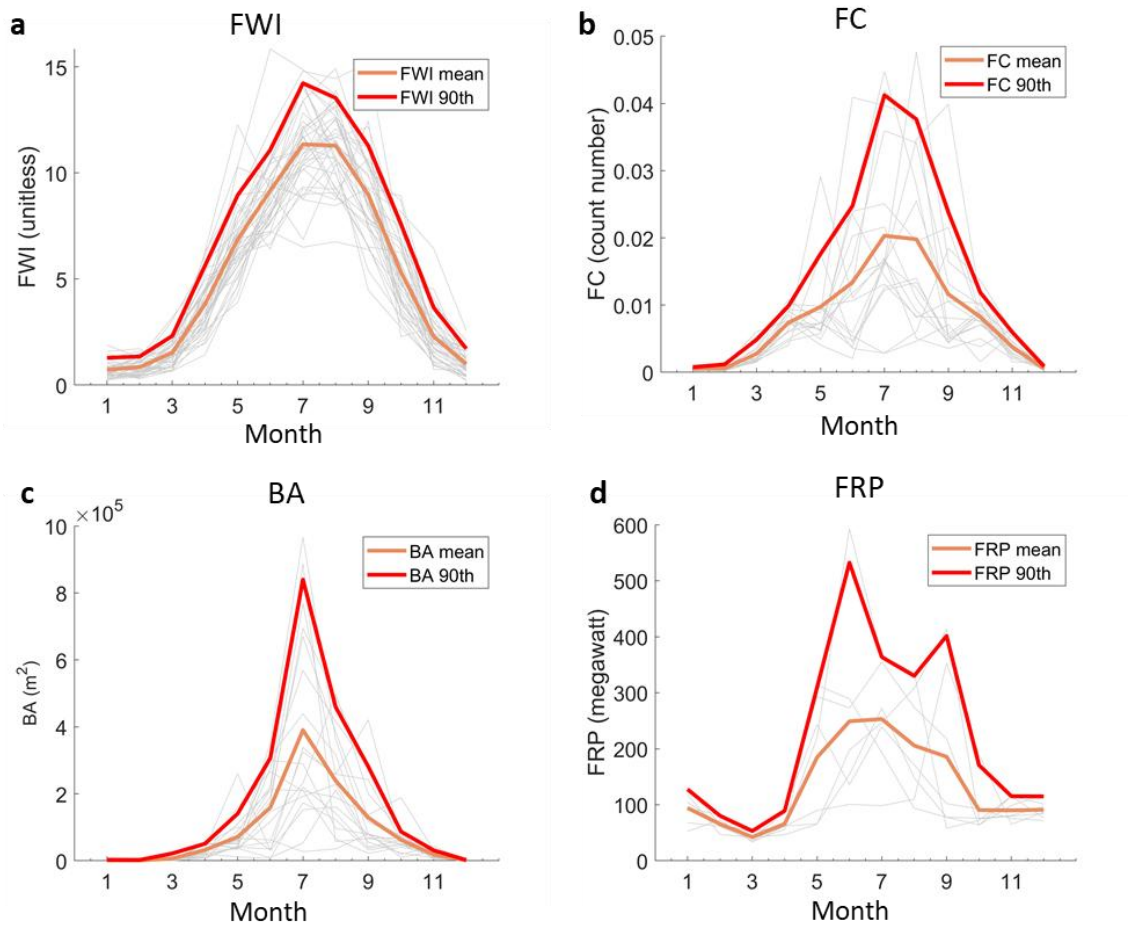

Fig. S1. Averaged seasonal cycle of fire proxies in Canada. Time series of annual monthly mean (a) FWI (unitless, 1981-2020) and (b) FC (fire count, 2003-2020), (c) BA (m^2, 2001-2020) and (d) FRP (megawatt, 2003-2020). Red dashed lines represent the 90th percentile of fire proxies, orange solid lines represent mean fire proxies, and gray lines represent monthly mean fire in every year.

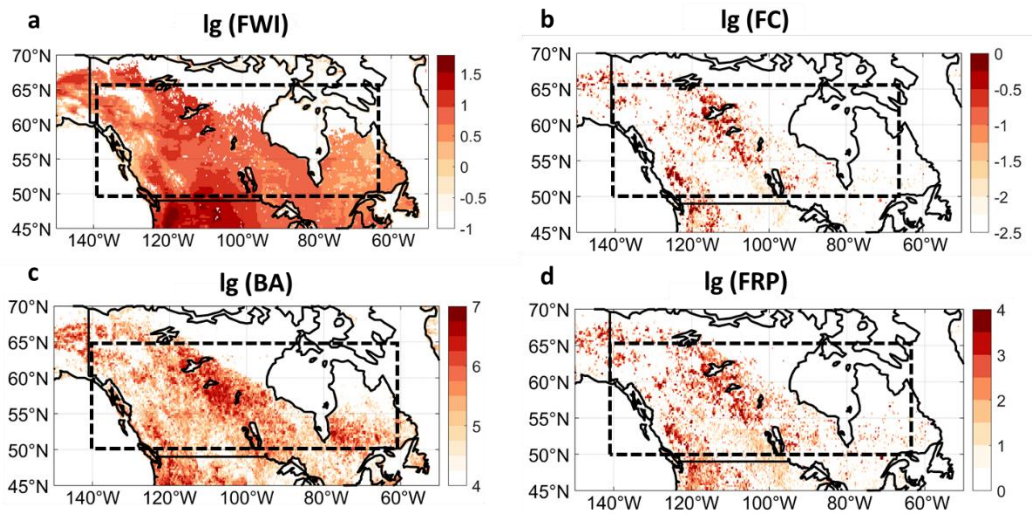

Fig. S2. Spatial distribution of fire activity proxies during the peak season in Canada (boreal summer, JJA). (a) Fire weather index (FWI, unitless, 1981-2020), (b) Fire count (FC, count number, 2003-2020), (c) Burned area (BA, m^2, 2001-2020), and (d) Fire radiative power (FRP, megawatt, 2003-2020). For clearer display, all physical quantities are expressed in logarithm scale with the base of 10 (expressed as lg). Dashed black boxes represent the area of Canada (50°-65°N, 60-140°W). FWIs corresponding to climatological Normalized Difference Vegetation Index<0.1 from 1981 to 2015 are removed (set to NaN), as those below this threshold typically correspond to barren soil without plants (Fang et al., 2004).

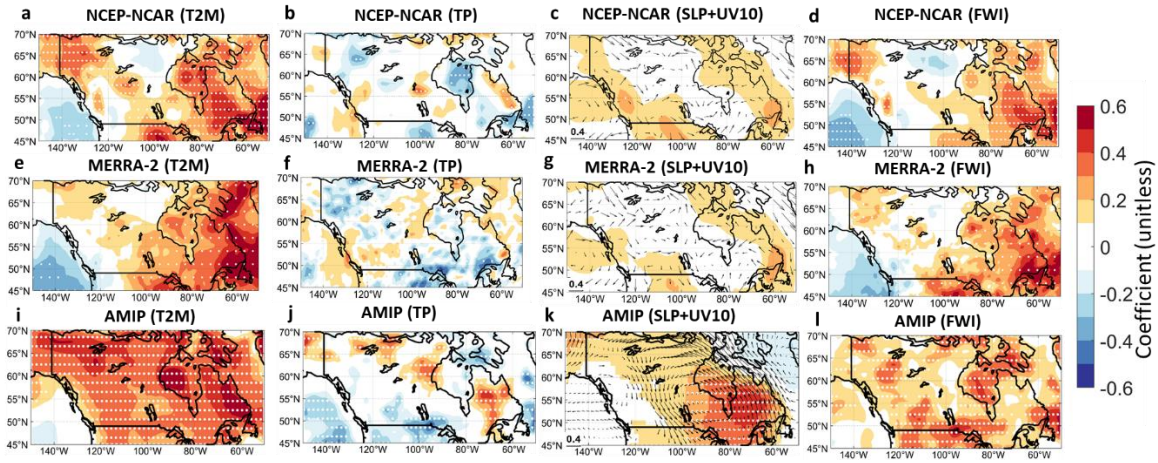

Fig. S3. Correlation between meteorological variables in Canada and North Atlantic SST in NCEP, MERRA-2 reanalysis datasets and AMIP simulation. The distribution of correlation coefficients between JJA meteorological variables and JJA North Atlantic SST in the (a-d) NCEP-NCAR reanalysis datasets, (e-h) MERRA-2 reanalysis datasets, and (i-l) CMIP6 AMIP. The meteorological variables include (a, e, i) T2M, (b, f, j) TP, (c, g, k) SLP (shaded) +U10+V10 (arrows), and (d, h, l) FWI calculated by RFR models. Before the correlation coefficients are determined, all of the time series were detrended. The area with white dots passes the significance test of $p \leq 0.1$ by Student's *t*-test.

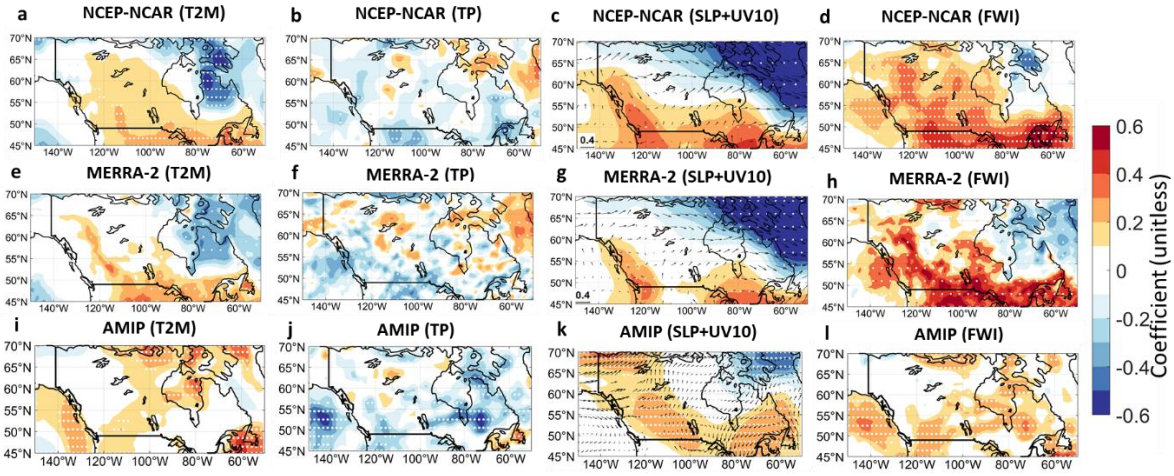

Fig. S4. Correlation between meteorological variables in Canada and Barents SIC in NCEP, MERRA-2 reanalysis datasets and AMIP simulation. The distribution of correlation coefficients between JJA meteorological variables and MJJ Barents SIC in the (a-d) NCEP-NCAR reanalysis datasets, (e-h) MERRA-2 reanalysis datasets, and (i-l) CMIP6 AMIP. The meteorological variables include (a, e, i) T2M, (b, f, j) TP, (c, g, k) SLP (shaded) +U10+V10 (arrows), and (d, h, l) FWI calculated by RFR models. The correlation coefficients are multiplied by -1 to indicate the Barents SIC reduction. Before the correlation coefficients are determined, all of the time series were detrended. The area with white dots passes the significance test of $p \leq 0.1$ by Student's *t*-test.

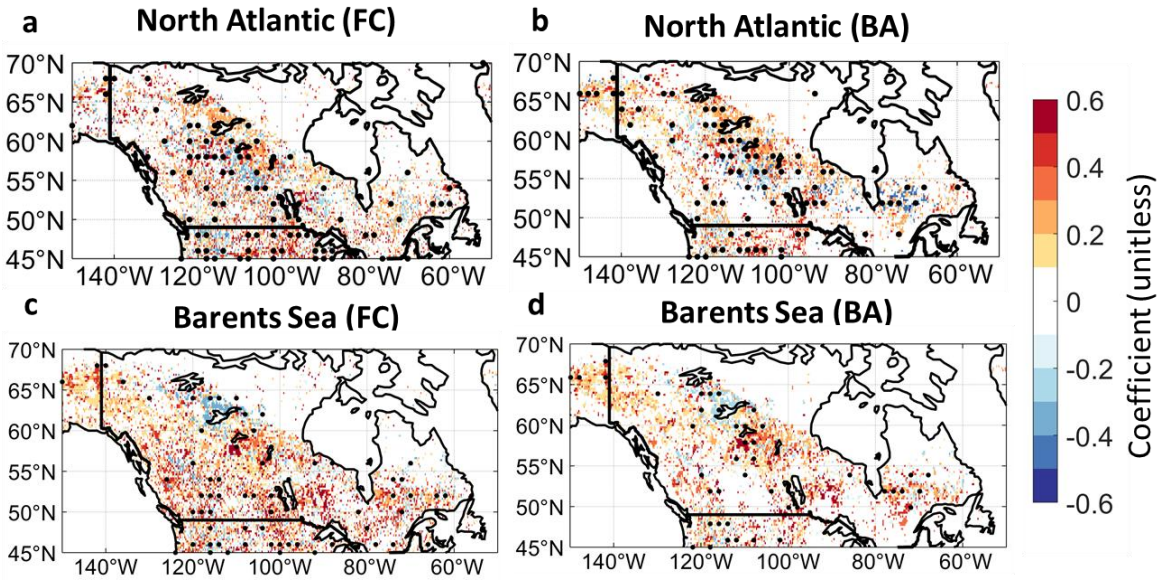

Fig. S5. Correlation between various fire proxies and North Atlantic SST/Barents SIC variability. (a, b) The distribution of correlation coefficients between JJA North Atlantic SST and (a) JJA FC (2003-2019) and (b) JJA BA (2001-2019). (c, d) The distribution of correlation coefficients between MJJ Barents SIC and (c) JJA FC (2003-2019) and (d) JJA BA (2001-2019). Before the correlation coefficients are determined, all of the time series were detrended. The correlation coefficients in (c) and (d) are multiplied by -1 to indicate the Barents SIC reduction.The area with black dots passes the significance test of $p \leqslant 0.1$ by Student's *t*-test.

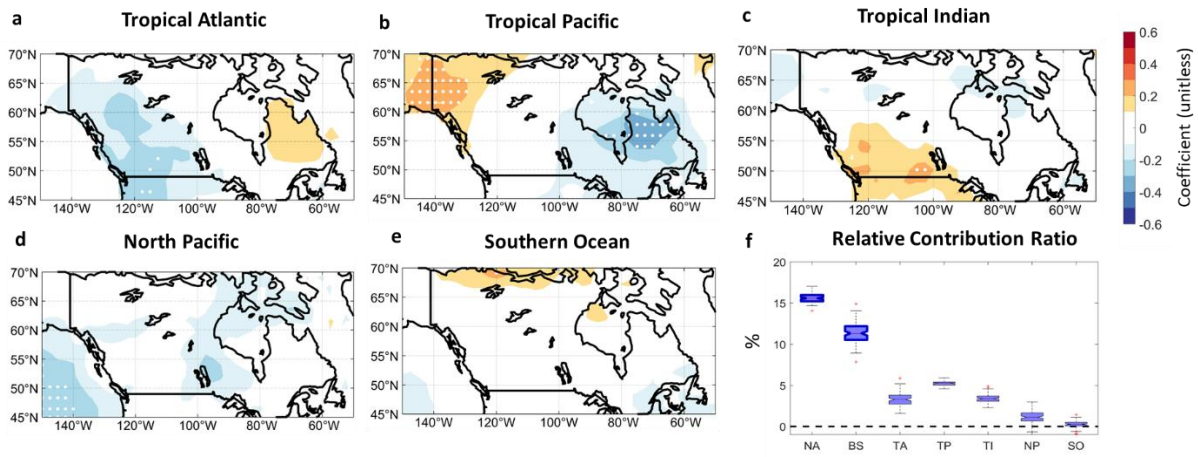

Fig. S6. Correlation patterns between other major ocean basin variability and FWI, and their relative contributions to FWI variability. The distribution of correlation coefficients between RFR based FWI and corresponding SST in various OBEs for (a) Tropical Atlantic OBE (10°S-10°N, 10°W-60°W) , (b) Tropical Pacific OBE (10°S-10°N, 80°W-130°W), (c) Tropical Indian OBE (10°S-10°N, 50°E-100°E), (d) North Pacific OBE (25°N-45°N, 170°E-140°W), (e) Southern Ocean OBE (60°S-80°S, 180°W-180°E), and (f) Contribution of unite change of North Atlantic SST (NA, ℃), Bering Sea SIC (BS, %), Tropical Atlantic SST(TA, ℃), Tropical Pacific SST (TP, ℃), Tropical Indian SST (TI, ℃), North Pacific SST (NP, ℃), and Southern Ocean SST (SO, ℃) to the change of JJA Canada FWI ratio (%). The black dotted line represents neutral FWI change. The bold blue boxes indicate significance of p-value $\leqslant$ 0.1 by Student's *t*-test.

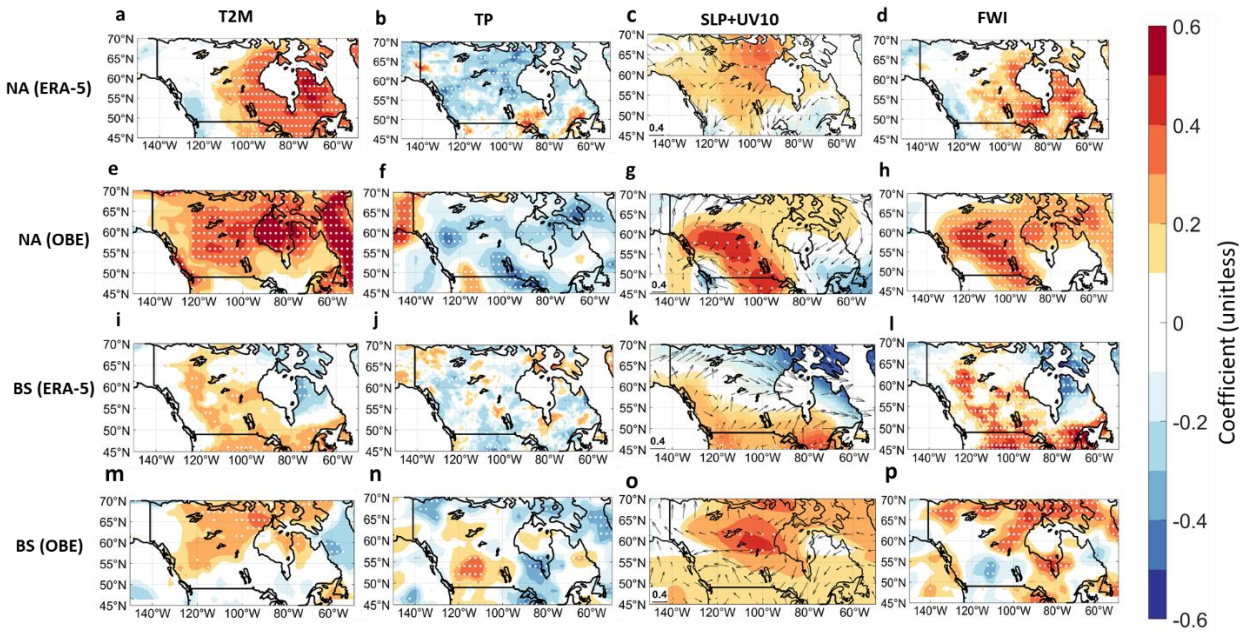

Fig. S7. Correlation between meteorological variables in Canada and North Atlantic SST/Barents SIC in ERA-5 reanalysis datasets and model simulation. (a-h) The distribution of the correlation coefficients between JJA meteorological variables and JJA North Atlantic SST in (a-d) the ERA5 reanalysis (1980-2019), and (e-h) similar to a-d, but for the OBE simulation. (i-p) The distribution of the negative correlation coefficients between JJA meteorological variables and MJJ Barents SIC in (i-l) the ERA5 reanalysis (1980-2019), and (m-p) similar to i-l, but for the OBE simulation. (a, e, i, m) T2M, (b, f, j, n) TP, (c, g, k, o) SLP (shaded) +U10+V10 (arrows), and (d, h, l, p) FWI calculated by RFR models. Before the correlation coefficients are determined, all of the time series were detrended. The correlation coefficients in (i) and (p) are multiplied by -1 to indicate the Barents SIC reduction. The area with white dots passes the significance test of $p \leqslant 0.1$ by Student's t-test.

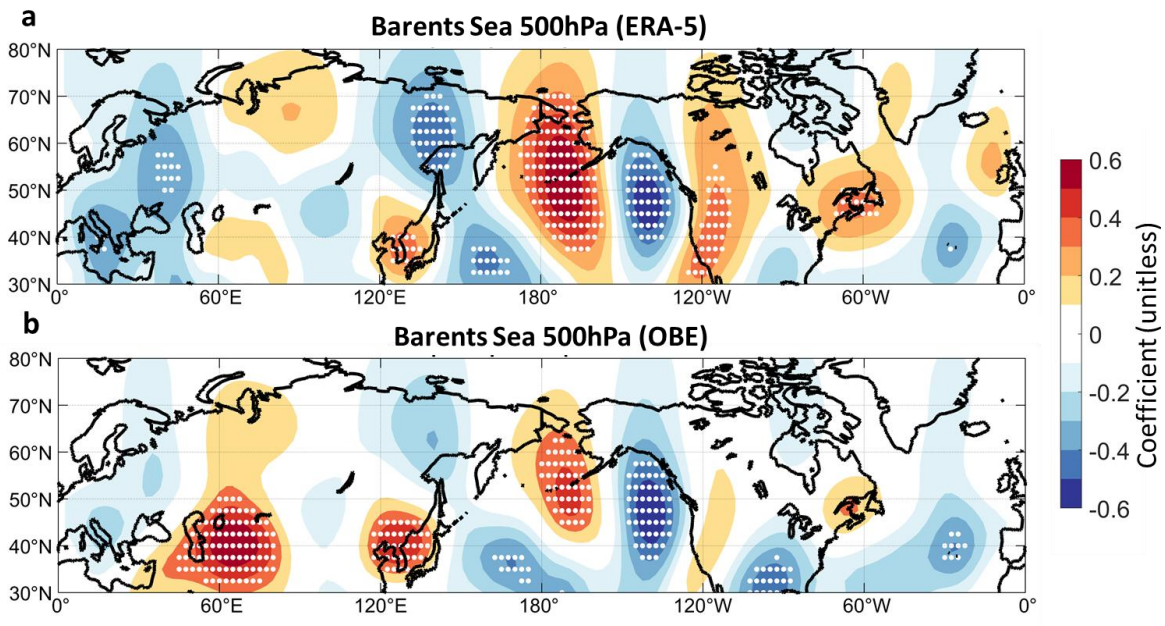

Fig. S8. Correlation between the stream function and Bering SIC. The distribution of correlation coefficients between JJA 500 hPa stream function and MJJ Bering SIC in the (a) ERA5 reanalysis (1980-2019) and (b) OBE. The correlation coefficients are multiplied by -1 to indicate the Barents SIC reduction. Before the correlation coefficients are determined, all of the time series were detrended. The area with white dots passes the significance test of $p \leqslant 0.1$ by Student's *t*-test.

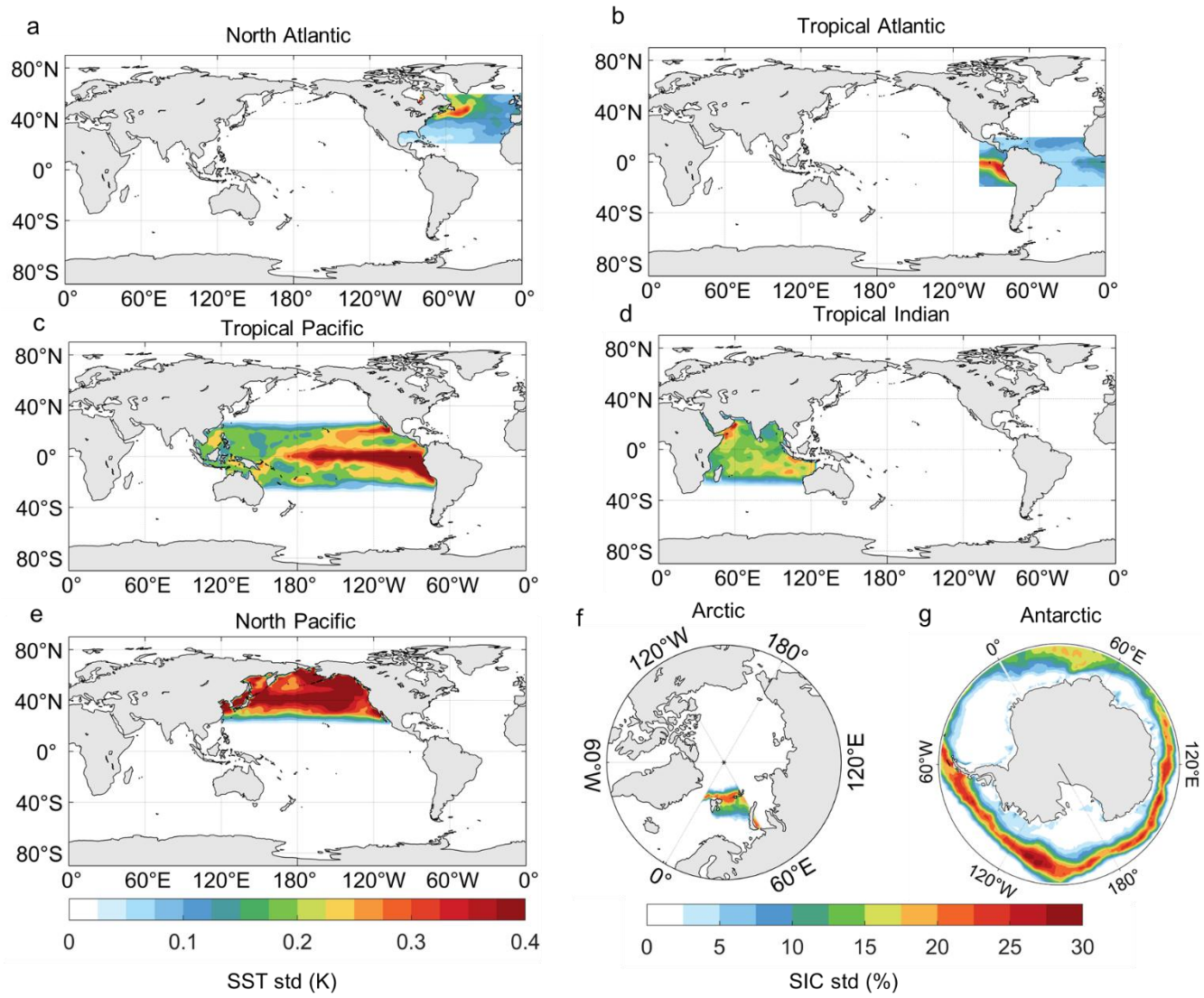

Fig. S9. SST and SIC variability in OBE with different forcings. The distribution of SST standard deviation in the (a) North Atlantic OBE, (b) Tropical Atlantic OBE, (c) Tropical Pacific OBE, (d) Tropical Indian OBE, and (e) North Pacific OBE. The distribution of SIC standard deviation in the (f) Arctic OBE and (g) Antarctic OBE.

References

1. Boucher et al. IPSL IPSL-CM6A-LR model output prepared for CMIP6 CMIP historical. Version 20180803. *Earth System Grid Federation* (2018).
2. Danabasoglu G. NCAR CESM2 model output prepared for CMIP6 CMIP historical. Version 20190401. *Earth System Grid Federation* (2019).
3. Fang, J. Y., Piao, S. L., He, J. S. & Ma, W. H. Increasing terrestrial vegetation activity in China, 1982-1999. *Science China Life Sciences, 47*, 229-240 (2004).
4. Krasting et al. NOAA-GFDL GFDL-ESM4 model output prepared for CMIP6 CMIP historical. Version 20190726. *Earth System Grid Federation* (2018).
5. Li L. CAS FGOALS-g3 model output prepared for CMIP6 CMIP historical. Version 20190818. *Earth System Grid Federation* (2019).
6. NASA Goddard Institute for Space Studies (NASA/GISS). NASA-GISS GISS-E2.1G model output prepared for CMIP6 CMIP historical. Version 20190908. *Earth System Grid Federation* (2018).
7. Ridley, J., Menary, M., Kuhlbrodt, T., Andrews, M. & Andrews, T. MOHC HadGEM3-GC31-LL model output prepared for CMIP6 CMIP historical. Version 20190624. *Earth System Grid Federation* (2019).
8. Seland et al. M. NCC NorESM2-LM model output prepared for CMIP6 CMIP historical. Version 20190920. *Earth System Grid Federation* (2019).
9. Swart et al. CCCma CanESM5 model output prepared for CMIP6 CMIP historical. Version 20190429. *Earth System Grid Federation* (2019).
10. Tatebe, H, Watanabe, M. MIROC MIROC6 model output prepared for CMIP6 CMIP historical. Version 20181212. *Earth System Grid Federation* (2018).
11. Vordoire, A. CMIP6 simulations of the CNRM-CERFACS based on CNRM-CM6-1 model for CMIP experiment historical. Version 20180917. *Earth System Grid Federation* (2018).
12. Wu et al. BCC BCC-CSM2MR model output prepared for CMIP6 CMIP historical. Version 20181126. *Earth System Grid Federation* (2018).
13. Yukimoto et al. MRI MRI-ESM2.0 model output prepared for CMIP6 CMIP historical. Version 20190222. *Earth System Grid Federation* (2019).

14. Ziehn et al. CSIRO ACCESS-ESM1.5 model output prepared for CMIP6 CMIP historical. Version 20191115. *Earth System Grid Federation* (2019).